A time-domain model for unsteady upwind sail aerodynamics using the indicial response method

(article starts on next page)

A time-domain model for unsteady upwind sail aerodynamics using the indicial response method

Adam Persson [a,b,*], Lars Larsson [b], Christian Finnsgård [a]

[a] *RISE Research Institutes of Sweden AB, Division Safety and Transport, Maritime, Göteborg, 400 22, Sweden*
[b] *Chalmers University of Technology, Mechanics and Maritime Sciences, Marine Technology, Göteborg, 412 96, Sweden*

ARTICLE INFO

ABSTRACT

For the design of sailing vessels, the use of Dynamic Velocity Prediction Programs is expanding, as naval architects start to consider the effects of waves and varying wind conditions in order to design faster, safer and more efficient vessels. Many models that predict the unsteady hydrodynamic response are available, but for sail aerodynamics, few models have been presented, and the quasi-steady assumption is instead commonly used. The aim of this paper is to develop a time-domain model for unsteady sail aerodynamics that can handle arbitrary motions and requires only limited input. The proposed model is based on the Indicial Response Method, with specific adaptations to handle the additional complexity of sail aerodynamics. The model's predictive performance is evaluated against URANS CFD results for several cases of increasing complexity. This includes a 3D upwind sail plan subjected to pitching motion, where comparisons are also made with the common quasi-steady (Q-S) assumption. Compared to this, the proposed model delivers significantly better predictions for the amplitude of lift, thrust and sideforce. However, the drag amplitude is over-predicted by the model, and as a result, there is a significant misprediction of thrust phase. While there is a need to improve the prediction of unsteady drag, this paper shows that the model represents a significant improvement over the Q-S assumption, for unsteady performance prediction on timescales shorter than the wave period.

1. Introduction

At the core of any Velocity Prediction Program (VPP) lie models that describe the aero- and hydrodynamic forces acting on a vessel. The choice of models is contingent upon the specific physical phenomena to be represented and the desired level of precision, ranging from simple semi-empirical relationships to extensive response-surface models derived from either experimental (EFD) or computational fluid dynamics (CFD) data. However, a significant proportion of existing models are steady-state, meaning that they neglect the additional forces created by the motions of a vessel.

The subset of unsteady models, that can account for the motions of a vessel, is considerably smaller. In previously presented dynamic VPPs (DVPP) various approaches have been proposed to model the effect of waves and motion on the hydrodynamic forces. Larsson (1990) used strip theory to compute the added resistance in waves, subsequently adding this resistance component to the still-water resistance. In the DVPPs developed by Ottosson et al. (2002) and Day et al. (2002), the added resistance and vessel motions in waves are computed with quasi-2D strip-theory, while Harris (2005) combined an unsteady panel code with strip theory. Horel and Durand (2019) combined a coefficient-based model for manoeuvring forces with a Boundary Element Method (BEM) for wave damping. Kerdraon et al. (2020) used a similar method to account for wave forces, but with CFD-based response surfaces for the manoeuvring forces, complemented with a quasi-steady (QS) Vortex Lattice Method (VLM) for appendage forces.

An alternative approach is to compute the hydrodynamic forces with Unsteady Reynolds Averaged Navier–Stokes (URANS) CFD, coupled with a rigid body motion (RBM) solver, to solve the forces and vessel motions in the time domain. Such methods have been presented by several authors (Azcueta, 2002; Roux et al., 2008; Böhm and Graf, 2010; Levin and Larsson, 2017; Persson et al., 2020) and can provide increased accuracy over simplified models, while reducing the need for empirically derived coefficient-based models or costly precomputed response surfaces.

While many different models for unsteady hydrodynamic forces have been proposed, for aerodynamic force models, the scope of previously published research is smaller. In some of the references mentioned above (Azcueta, 2002; Levin and Larsson, 2017) the unsteady effects on aerodynamic forces have been neglected altogether, but a

quasi-steady approach is often utilised, meaning that the vessel motions are considered when computing the apparent wind speed and apparent wind angle. These values are then used to interpolate in tabulated static force coefficients, either empirically derived, such as the coefficients used by the Offshore Racing Congress VPP (ORC, 2023), or pre-computed using CFD.

A notable exception is described by Roux et al. (2008), where a lifting surface method is used for the sails, modelling the wake using an unsteady Vortex Element Method. Roux et al. (2008) notes that this model has been demonstrated to successfully describe dynamic effects in detail, for realistic sailing conditions.

Quasi-steady, coefficient-based models have been shown to be inadequate for predicting sail forces in unsteady conditions. In Gerhardt et al. (2008) a rigid 2D mainsail section, subjected to harmonic oscillations, was studied. Pressure distributions and forces predicted with unsteady thin-airfoil theory were compared to wind tunnel measurements. Gerhardt et al. concluded that an unsteady aerodynamic model should be used for performance prediction at timescales shorter than the pitching period. Fossati and Muggiasca (2010) investigated the unsteady aerodynamics of a rigid 3D sail plan, subjected to harmonic pitching, using wind tunnel tests. Fossati and Muggiasca also identified differences between the unsteady forces and their quasi-steady equivalent, with significant hysteresis found in the unsteady results.

In a series of papers, Augier et al. (2012, 2013, 2014) studied the unsteady aerodynamics of a J/80 sail plan using a potential flow solver with Fluid-Structure Interaction (FSI), and compared these results to full-scale experimental measurements, leading to several important conclusions. Augier et al. confirm that the unsteady aerodynamic forces deviate from those predicted with quasi-steady theory. The hypothesis that a pitch motion can be decomposed into two translatory motion components, surge and plunge, is confirmed. The authors show that considering surge motion only does not model unsteady effects, resulting in under-predicted amplitude and no hysteresis. Importantly, by comparing predictions with FSI to corresponding predictions with rigid sails, the authors provide some support for neglecting FSI, showing that the qualitative behaviour is similar, and the quantitative differences are small for all but the highest reduced frequencies.

While the modelling of unsteady sail aerodynamics is underdeveloped in general, and the commonly utilised models have been shown to be deficient, a few more comprehensive models have been proposed, notably by Fossati and Muggiasca (2010) and Gerhardt et al. (2011).

Fossati and Muggiasca (2010) proposed two different time-domain numerical models. Both of these models depend on the availability of forced motion data for a pitching 3D sail plan, for a range of reduced frequencies. The first model proposed by Fossati and Muggiasca assumes that the sail force coefficients can be described as a nonlinear polynomial function of the instantaneous apparent wind angle and its time derivative. The polynomial coefficients are identified from the forced motion data, with one set of coefficients required for each reduced frequency. The second model considers the sail plan as a mechanical system (i.e. a rheological model) composed of a spring and a damper in series, with the input again being the instantaneous apparent wind angle and its time derivative. The authors conclude that both models seem to reproduce the effects found in the experimental investigation. However, the complexity of producing forced motion calibration data required, over a wide range of reduced frequencies, is a hindrance to the practical use of these models.

Gerhardt et al. (2011) presented an extended unsteady thin airfoil theory for interacting 2D jib-mainsail sections, oscillating with a harmonic motion perpendicular to the incident flow direction. The theory is validated against unsteady wind tunnel test results for a high aspect-ratio (quasi-2D) jib-mainsail combination, and its applicability for yachts is shown using an International Americas Cup Class (IACC) yacht as a test case. In particular, the decomposition of the pitching motion of a yacht sailing upwind in waves into surge and plunge is

discussed. For the IACC yacht case, it is shown that the surge component can be treated quasi-steadily, while the plunge component requires careful treatment. As is described by Gerhardt et al., the plunging motion generates a time-varying angle of attack and thus, also time-varying bound circulation, resulting in continuous shedding of vorticity into the wake from the trailing edge. The unsteady wake of each sail is represented by a planar vortex sheet. Employing a tangential flow condition on the sails, the unsteady bound vorticity distributions are given by two coupled integral equations. The bound vorticity distributions are represented by truncated, modified Glauert series, leading to a system of linear equations which is solved to obtain the Glauert coefficients. From these, the unsteady bound vorticity distributions can be reconstructed, and subsequently, pressure distributions and aerodynamic forces can be obtained. The predictions obtained with the extended theory were validated against results from wind-tunnel tests of oscillating sail models, showing significantly improved predictions compared to the quasi-steady approach. Application of the theory to an IACC yacht (as used in the America's Cup between 1992 and 2007) case and a Deed-of-Gift (DoG) multihull yacht as used in the America's Cup in 2010, showed that an unsteady lift amplitude of 5–10% can be expected depending on the conditions.

The purpose of this paper is to investigate how existing models from the aerospace field can be utilised to model the unsteady aerodynamics of upwind sails, aiming to create a time-domain model that can handle arbitrary motions, and requires only limited, low-cost computational (2D) input to define the dynamic response of the section. Except for the function describing the dynamic response, all other model parameters can be derived from a sailplan drawing. The model should predict the change in forces due to motion, allowing correction of steady-state sail coefficients, such as those presented by ORC (2023), to consider dynamic effects.

2. Theoretical background

The prediction of unsteady aerodynamics is a problem of great practical relevance in the field of aeronautics, both for fixed-wing aircraft where for example flutter, gust response and manoeuvring characteristics must be predicted. The ability to predict unsteady aerodynamic effects is also important for the design of reliable helicopter rotor systems, which in normal operation encounter a range of unsteady flow conditions. These applications have motivated significant research into this problem.

The classical unsteady aerodynamic problem of a thin airfoil, subject to small harmonic lateral oscillations in a uniform flow of incompressible fluid, was first approached by Glauert (1930), but finally solved by Theodorsen (1949). Other researchers reached the same result independently, as mentioned by Bisplinghoff et al. (1983).

Theodorsen's theory is given in the frequency domain and separates the aerodynamic response into circulatory and non-circulatory parts. The circulatory part describes the influence that the shed wake vorticity has on the downwash velocity on the airfoil, while the non-circulatory part results from the acceleration of the surrounding fluid, i.e. added mass. For a thin airfoil (represented by a flat plate) with chord length $c = 2b$, and harmonically varying plunge displacement (Y) in an incompressible fluid with density ρ and steady flow with velocity U, Theodorsen's theory gives lift per unit span (2D) as shown in Eq. (1).

$$L = -\pi\rho b^2 \ddot{Y} + 2\pi\rho U^2 b \left[\frac{-\dot{Y}}{U} + \alpha \right] C(k) \tag{1}$$

In the equation above, the first term describes the non-circulatory response, while the second term gives the circulatory response. $C(k)$ is a complex-valued transfer function, known as Theodorsen's function, that relates the change in angle of attack to the aerodynamic response (pressure distribution, lift and pitching moment). Theodorsen's function accounts for the influence of the shed wake vorticity on the circulatory contribution, and depends only on the reduced frequency $k = \frac{\omega b}{U}$, where ω is the angular frequency of the harmonic plunge oscillation.
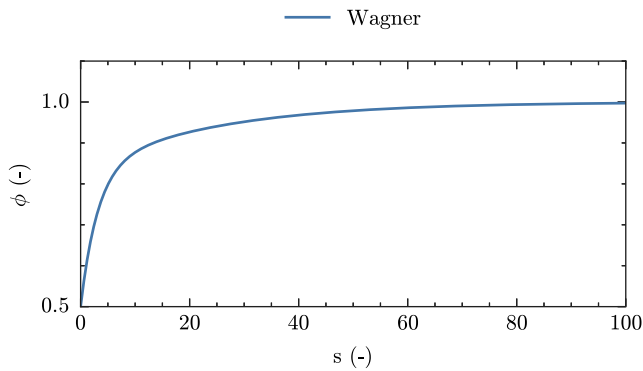
Fig. 1. Visualisation of the Wagner function (Jones approx.).

Fig. 2. Visualisation of the Duhamel superposition.

Fig. 3. 2D NACA0006 airfoil. Motion directions indicated.

Fig. 4. 2D sail section. Motion directions indicated.

While Theodorsen's original theory has been validated for harmonic motion (Leishman, 2006), and a modified version of the theory that uses Fourier series to approximate the aerodynamic response to general periodic motion has been presented by Ōtomo et al. (2021), the general applicability of Theodorsen's theory is limited by the requirement for periodic motion, as well as the assumptions inherited from the underlying thin airfoil theory. For the analysis of problems involving arbitrary, non-periodic motion, another approach is required. Wagner (1925) studied the problem of the unsteady response of a thin airfoil experiencing a step change in angle of attack. Using thin airfoil theory, Wagner derived the so called Wagner function $\phi(s)$, which describes the indicial response of a thin airfoil as a function of s, a nondimensional time, defined as $s = 2Ut/c$. A visualisation of the Wagner function is shown in Fig. 1. The Wagner function can be used together with the Duhamel (superposition) integral to describe the response of an airfoil to arbitrary motions. A graphical overview of this process is shown in Fig. 2. Firstly, the arbitrary motion is represented as a series of step changes. Each subsequent step change adds a scaled instance of the Wagner function, and the unsteady lift at a given time can then be obtained by superposing these curves along the vertical line. The derivation is reproduced in full by Bisplinghoff et al. (1983), but the resulting expression for unsteady lift as a function of angle of attack, $\alpha(t)$, is given in Eq. (2) on a form corresponding to that given above for Theodorsen's theory. A dummy time variable, σ, is introduced for integration.

$$L = -\pi \rho b^2 \ddot{Y}$$
$$+ 2\pi \rho U^2 b \left[\alpha(0)\phi(s) + \int_0^s \frac{d\alpha}{dt}(\sigma)\phi(s - \sigma)d\sigma \right] \quad (2)$$

While the Wagner indicial response function is based on thin airfoil theory, and thus introduces some limiting assumptions, the superposition principle shown above can be used with other indicial response functions (IRF). IRFs can, for example, be obtained from oscillatory experimental results (Leishman, 1993) or computed directly with CFD (Mccroskey and Goorjian, 1983; Lesieutre et al., 1994; Singh and Baeder, 1997; Ghoreyshi et al., 2012). This makes it possible to include the effects of viscosity as well as the interaction between several airfoil elements, and for some motions, also 3D effects can be included. This combination, using the Duhamel integral with an alternative IRF, can be described as a 'modern' indicial response method (IRM). In the following section, the implementation of this method and the adaptations necessary for its application to sails will be described.

3. Method

As is concluded in Section 1, the existing models for unsteady sail aerodynamics are not suitable for the purpose of this study, as they eithe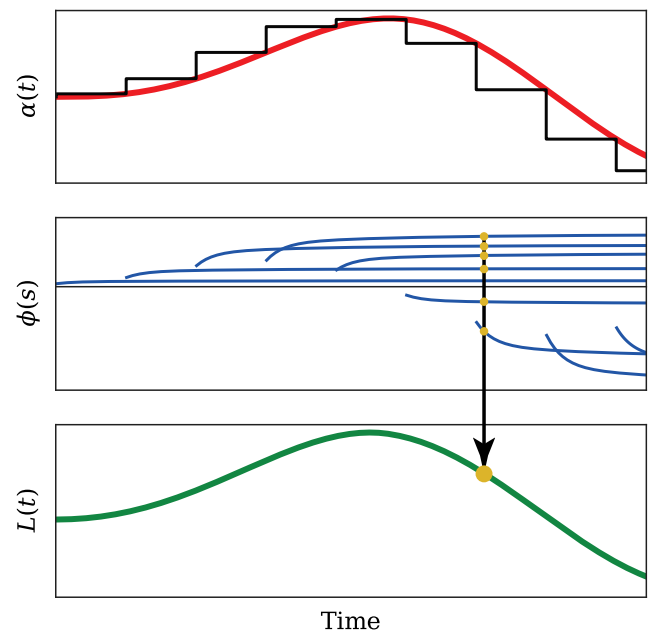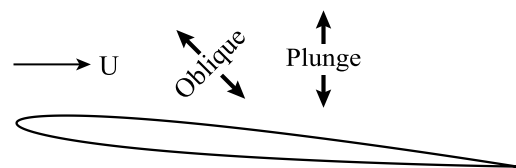r require a detailed geometrical definition of the sailplan, or are limited to periodic motion. However, there are models from the aerospace field that could be suitable, in particular the indicial response method (IRM). In this study, the modelling considerations that are specific to unsteady sail aerodynamics will be briefly reviewed, and adaptations of the IRM method will be presented to handle these considerations. Three geometries will be studied; a 2D NACA0006 airfoil (see Fig. 3); a 2D sail section, consisting of a jib and mainsail (see Fig. 4); and a 3D upwind sail plan again consisting of a jib and mainsail (see Fig. 7). The sail plan and the sail section have been derived from the scale-model flying shapes measured experimentally by Fossati et al. (2008), but have been slightly modified, with an increase of twist in the upper half of the jib and mainsail to reduce unsteady separation on the leeward side.
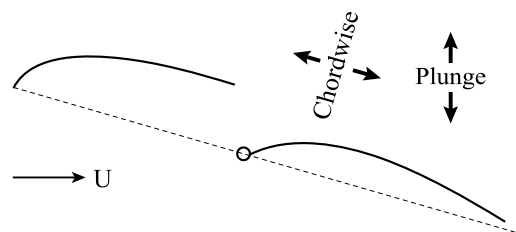
The implemented code will be verified using the plunge motion case for the NACA0006 airfoil, and the model performance will then be evaluated against 2D and 3D URANS CFD simulations, with 7 different cases studied, including different motion directions and reduced frequencies. In Figs. 3 and 4 the motion directions have been indicated. The cases have been selected in an attempt to allow separation of
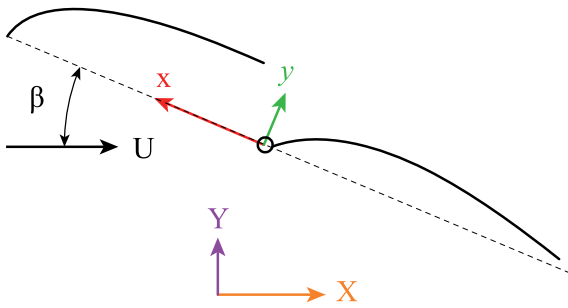
Fig. 5. Motion transformation from body-fixed to wind-aligned coordinate system, in a plane orthogonal to the mast.

different modelling aspects, allowing their relative importance to be evaluated, providing an indication of which areas should be prioritised in continued model development.

3.1. IRM for unsteady sail aerodynamics

Compared to the typical applications for IRM models, unsteady sail aerodynamics introduces some additional considerations. Sail sections are often heavily cambered and consist of two or more elements (jib and mainsail). The asymmetry due to camber introduces cross-coupling effects, and the multi-element configuration introduces interaction effects, changing the effective inflow angle to the sail section and altering the pressure distributions on the elements. This interaction is of critical importance for steady sail aerodynamics, and may also introduce significant effects for the unsteady response of the sail section. In this paper, the interaction effects are implicitly modelled by the CFD-derived IRF.

For some cases, the prediction of the unsteady variation of sail thrust can be important, such as for reaching or downwind sailing. The thrust of a sail is formed by projection of lift and drag with the apparent wind angle β onto the direction of motion of the yacht; therefore, for the prediction of unsteady thrust, both unsteady lift and drag must be predicted, in contrast to typical applications for IRM models, where unsteady drag is often neglected (Leishman, 1988).

Finally, the motion experienced by a sail is different from that encountered in typical applications, where plunge, angle-of-attack and flap angle variations are the dominating motion components (Leishman, 2006). For sail aerodynamics applications, the roll and pitch motion of the boat will result in the sail section experiencing a combination of surge and plunge motion. For upwind cases, where pitch is expected to be the dominating boat motion, the surge motion component of the sail section is significant.

The model implementation presented here has been developed for integration into a CFD-VPP procedure, such as that presented by the authors in Persson et al. (2020). It is necessary to transfer motion data from the CFD-VPP to the unsteady aerodynamics model. This is done by extracting the instantaneous velocity and acceleration in multiple local body-fixed coordinate systems (x_i, y_i, z_i). One coordinate system is defined for each strip, with the origin placed at the area centroid height d_w. Being body-fixed, the coordinate systems follow the 6DOF motions of the vessel, meaning that computations of velocities and angle of attack are made in a plane orthogonal to the mast, heeling with the vessel. The extracted acceleration values are then used directly to compute added mass forces (see Section 3.1.4), but the velocities must be processed to be consistent with the IRM model, as described in Section 3.1.1.

In the following sections, the approach taken to discretise the sailplan and process the yacht motions will be discussed, and the models used to predict the different force contributions will be presented.

3.1.1. Motion decomposition and discretisation

The indicial response method was originally developed to model the unsteady response of a 2D airfoil section subjected to in-plane motion; either plunge displacement, angle-of-attack variation, or a combination of the two. Thus, the use of the IRM method for the 2D cases presented in this paper is relatively straightforward, requiring only the transformation of the body-fixed velocities to a coordinate system aligned with the freestream flow, as shown in Fig. 5 and Eqs. (3a) and (3b). This transformation is necessary since the IRM model uses the unsteady angle of attack α' and unsteady wind speed U' to compute the unsteady aerodynamic forces. This is done as shown in Eqs. (4b) and (4a).

$$\dot{X} = \dot{y}\sin\beta - \dot{x}\cos\beta \tag{3a}$$

$$\dot{Y} = \dot{x}\sin\beta + \dot{y}\cos\beta \tag{3b}$$

$$U' = U - \dot{X} \tag{4a}$$

$$\alpha' = \arctan\frac{-\dot{Y}}{U'} \tag{4b}$$

The 3D test case, representing a yacht sailing upwind in waves, has a more complex motion, rotating around a transverse axis located close to the yacht centre of gravity. In order to represent the geometry of the 3D sailplan a strip approximation is used. To enable repeatable discretisation and simplify geometry processing, an automated process has been developed using Grasshopper, a graphical scripting environment for the Rhinoceros 3D CAD software that includes a variety of tools for geometry handling and analysis. These tools are utilised to compute the required quantities described below. The 3D sailplan geometry is discretised as a finite number of strips, where the desired number of strips is provided as input by the user. All strips have equal height h, determined from the number of strips and the overall span of the sailplan. The projected strip area a is computed by projecting the subdivided sail surfaces onto the centre-plane of the yacht. The area centroid height d_w of the strip is computed, and the chord length c is then obtained as the distance between the leading edge of the jib and the trailing edge of the mainsail at the area centroid height.

The sensitivity to discretisation has been preliminarily investigated by graphical comparison of the forces predicted with 5 strips, as used for final 3D computations shown in Section 4.4, with an alternative discretisation using 10 strips. The results are shown in Fig. 6. Small differences can be seen for both lift, drag and sideforce amplitude, with a maximum difference of 2.5%, while for thrust, a difference of 10% is found.

The motion parameters (velocity and acceleration) are extracted from the reference CFD simulation, in a local, body-fixed coordinate system (x_i, y_i, z_i) for each strip, located at the strip centroid height d_w. The linear velocities and accelerations are extracted in this coordinate system, reducing the 3D pitching motion to a linear translation. The velocity and acceleration are taken as constant over the height of each strip. The local velocities, $\dot{x}_i$ and $\dot{y}_i$, are then used to compute instantaneous angle of attack and instantaneous wind speed in the same way as for the 2D case, see Fig. 5 and Eqs. (3a) and (3b).

3.1.2. Modelling of circulatory unsteady lift

The indicial response method is based on the fundamental assumption that the flow can be linearised with respect to the forcing function. Considering the unsteady lift coefficient $C_l(t)$, and assuming this to be a smooth function of the angle of attack α; if the angle of attack varies about a mean value α_m with $\Delta\alpha$, we can approximate the time-varying behaviour of C_l as a first-order Taylor series expansion, as is shown in Eq. (5).

$$C_l(t) = C_l(\alpha = \alpha_m, t = t_0) + \frac{\partial C_l}{\partial \alpha}\Delta\alpha \tag{5}$$

Assuming that $\partial C_l/\partial \alpha$ is a linear time invariant response, meaning that it does not depend on α but only on the time after which the change
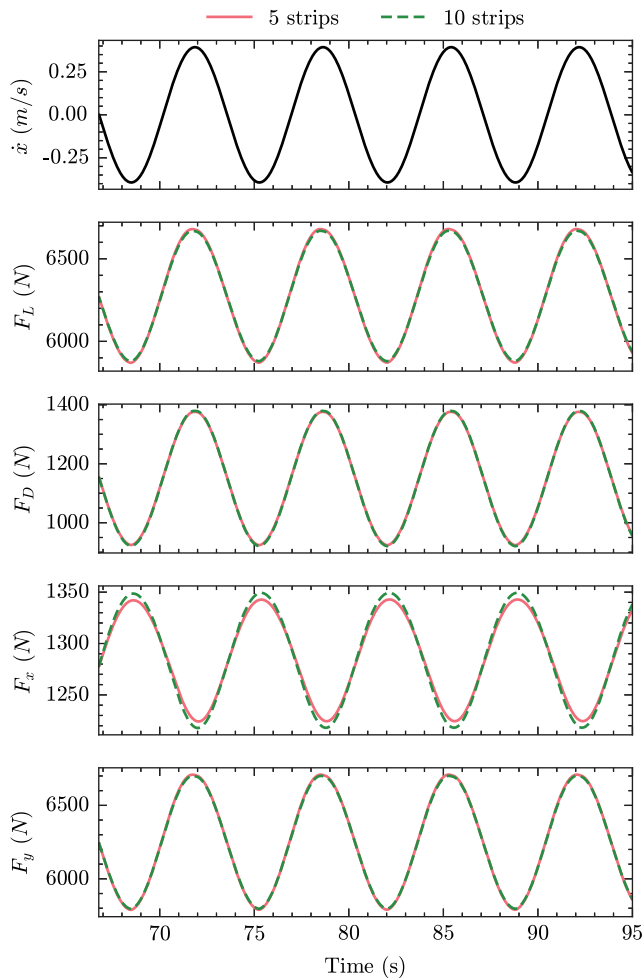
Fig. 6. Discretisation sensitivity; comparison of forces predicted using 5 and 10 strips for discretisation.
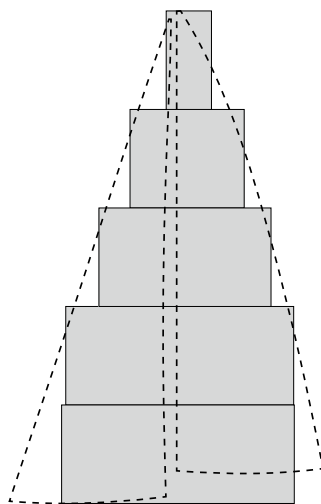

Fig. 7. Sailplan strip discretisation, with 5 strips. Dotted black line shows original outline.

in angle of attack ($\Delta\alpha$) is applied, then this can be written as shown in Eq. (6).

$$C_l(t) = C_l(t=0) + \frac{dC_l}{d\alpha}(t)\Delta\alpha = C_l(t=0) + \phi(t)\Delta\alpha \tag{6}$$

where $\phi(t)$ is the so-called indicial response function (IRF) of C_l to a unit step change of α. For arbitrary variations in α, we can use the Duhamel superposition integral to express $C_l(t)$ according to Eq. (7).

$$C_l(t) = \frac{dC_l}{d\alpha}\alpha(0)\phi(t) + \frac{dC_l}{d\alpha}\int_0^t \frac{d\alpha}{dt}(\sigma)\phi(t-\sigma)d\sigma \tag{7}$$

where σ is a dummy time variable for integration. The time-varying lift coefficient can subsequently be expressed as shown below (Eq. (8)).

$$C_l(t) = C_{l_\alpha}\left[\alpha(0)\phi(s) + \int_{s_0}^s \frac{d\alpha}{dt}(\sigma)\phi(s-\sigma)d\sigma\right] = \frac{dC_l}{d\alpha}\alpha_e(t) \tag{8}$$

The terms within the bracket can be viewed as an effective AoA that incorporates the effect of the velocities induced by the previously shed unsteady wake vorticity, called $\alpha_e(t)$.

In a discrete system, sampled at non-dimensional times $s = s, \sigma_i, \ldots, \sigma_1, s_0$ separated by a constant time-step Δs, the α_e term can be written as:

$$\alpha_e(s) = \alpha(s_0)\phi(s) + \sum_{i=1}^\infty \frac{d\alpha}{ds}(\sigma_i)\phi(s-\sigma_i)\Delta s \tag{9}$$

The first term above represents the downwash induced by the starting vortex created as the airfoil starts from $U = 0$. This term will be of waning influence as s grows large and the distance to the initial starting vortex increases. In this paper, it is assumed that the unsteady motion starts when the system is in a steady state, and thus, the first term in Eq. (9) is neglected. The resulting equation for $\alpha_e(s)$, as implemented with the Python programming language in vectorised form, is shown in Eq. (10).

$$\alpha_e(s) = \left[\Delta\vec{\alpha} \cdot \phi(s-\vec{\sigma})\right] \tag{10}$$

Here, $\Delta\vec{\alpha}$ is a vector containing the discrete change in angle of attack between subsequent time-steps for times $s = s, \sigma_i, \ldots, \sigma_1, s_0$ and $\vec{\sigma}$ is a vector containing all previous values of non-dimensional time. The unsteady change in lift coefficient $\Delta C_l(s)$ is then obtained by multiplying the force coefficient curve slope with the effective AoA from Eq. (10), as is shown in Eq. (11).

$$\Delta C_l(s) = \frac{dC_l}{d\alpha}\alpha_e(s) \tag{11}$$

3.1.3. Modelling of circulatory unsteady pressure drag

Most of the historical research on unsteady aerodynamics has focused on fixed-wing aeroelasticity, where any variation of drag due to the unsteady effects is irrelevant and thus can be neglected; but some research on unsteady drag has been carried out in order to construct comprehensive models of helicopter rotor aerodynamics. For this purpose, Leishman (1988) presented a model for the two-dimensional unsteady pressure drag under attached flow conditions, which is compatible with the Indicial Response Method for unsteady lift. The model uses the normal (C_N) and axial (C_A) force coefficients to compute the unsteady pressure drag, and requires some calibration, of the so-called suction recovery factor η, using steady experimental or computational results.

For sail force modelling, the use of normal and axial force coefficients is unconventional, making it difficult to implement the model suggested by Leishman (1988). Furthermore, the suction recovery factor η, which for typical helicopter rotor airfoil geometries is known to be around 0.95, is unknown for sail section geometries, further complicating the application of this model to yacht sails.

For the reasons above, the model proposed by Leishman (1988) is not used in this paper. Instead, the unsteady pressure drag is modelled in analogy with how induced drag is computed for a finite wing. The presence of motion will alter the effective angle between the flow and the section, causing a rotation of the lift vector. Since the lift and drag forces are evaluated relative to the undisturbed freestream direction, the rotated lift vector will have a longitudinal (drag) component, given by the projection of the instantaneous lift vector by the effective angle

of attack. This is taken to be the unsteady pressure drag contribution $\Delta C_{D,p}$, according to Eq. (12) where $C_{L,S}$ is the static lift coefficient, and the rightmost term corresponds to the unsteady instantaneous lift coefficient due to motion, see 3.1.2. It should be noted that only the circulatory components of the instantaneous lift are considered in the computation of unsteady pressure drag. The non-circulatory (added mass) components are considered separately, as is described in Section 3.1.4.

$$\Delta C_{D,p} = -\left(C_{L,S} + \frac{dC_l}{d\alpha}\alpha_e\right)\tan\alpha_e \tag{12}$$

3.1.4. Modelling of the added mass forces

There is a need to consider an extended range of reduced frequencies k for unsteady sail aerodynamics, compared to those typically studied in fixed wing aeroelasticity or rotor aerodynamics. While the 3D case studied here has a reduced frequency $k = 0.5$, other authors have noted (Gerhardt et al., 2011) that the reduced frequencies on yacht sail plans often exceed $k = 1$, and for some classes of yachts, with large chord length sails operating at low wind speeds, the reduced frequency can even approach $k = 2$.

With increasing k, the importance of added mass forces increases, and with the relatively large angles of attack seen on sails, also the surge component of the added mass forces can become significant. For this reason, it is necessary to expand the modelling of added mass beyond what is normally used for fixed wing elasticity or rotor aerodynamics applications, which only considers the added mass of a flat plate accelerated in the plunge direction (Leishman, 2006).

As a body is accelerated in a fluid, all the fluid surrounding the body will also have to be accelerated to some degree. While the fundamental interpretation of added mass is that it defines the work required to change the total kinetic energy of all surrounding fluid, it is instead often modelled as a specific volume of fluid accelerated with the same acceleration as the body, defined by the added mass coefficient λ. For a body with added mass coefficient λ, subjected to an acceleration $\dot{x}$ in a fluid of density ρ, the added mass force can be computed as $F_{AM} = \lambda\dot{x}\rho$.

For many simple shapes, the added mass coefficients have been derived analytically and are available in tabulated form (see, for example, Brennen (1982)), making the practical modelling of apparent mass for such shapes straightforward. But for more complex shapes, the added mass coefficients have to be calculated numerically. While URANS CFD is today the most common method used to numerically predict unsteady flow forces, it cannot be readily used to compute added mass coefficients, since it is difficult to separate the force contributions from fluid inertia from those caused by circulation and viscosity.

However, using a potential flow solver, a solution without the effects viscosity and circulation can be readily obtained, allowing the evaluation of added mass forces in isolation. The 2D grid-based potential flow method presented by Beckers and Eldredge (2022) can compute the added mass tensor for an arbitrary number of bodies of arbitrary (open or closed) shape. The coefficients of the added mass tensor of a body are obtained by computing the impulse components associated with a unit-valued translatory motion. Beckers and Eldredge have made an implementation of their method publicly available. The routine for computing added mass has been modified slightly, so that instead of computing the added mass coefficient matrix for each body moving separately, the total added mass of the bodies moving together is computed. The modified procedure has then been used to compute the added mass tensor for the airfoil and sail section.

The 2D added mass tensor is computed in the body-fixed coordinate system (x, y), see Fig. 5. The tensor contains four elements (see Eq. (13)), where the diagonal elements m_{xx} and m_{yy} describe the forces generated in x-direction by an acceleration in x-direction, and in y-direction by an acceleration in y-direction, respectively. The off-diagonal elements, $m_{xy} = m_{yx}$, describe the cross-coupling, i.e the forces

generated in the x-direction by an acceleration in y-direction and vice versa.

$$\lambda = \begin{bmatrix} m_{xx} & m_{xy} \\ m_{yx} & m_{yy} \end{bmatrix} \tag{13}$$

Many common geometries, such as circles and ellipses, are symmetric, and thus, the off-diagonal terms are zero ($m_{xy} = m_{yx} = 0$). However, this is not the case for the asymmetric sail-section, where significant cross-coupling occurs. The computed added mass tensors, for the NACA0006 airfoil and sail section, are shown in Equations (14) and (15).

$$\lambda = \begin{bmatrix} 0.0472 & 0.0 \\ 0.0 & 3.304 \end{bmatrix} \tag{14}$$

$$\lambda = \begin{bmatrix} 0.117 & 0.212 \\ 0.212 & 2.07 \end{bmatrix} \tag{15}$$

In order to reduce the amount of pre-computed input required, the added mass tensor is computed for a geometry with unit semi-chord. The added mass coefficients is then scaled with the square of the actual semi-chord length b^2, to account for the difference in chord length seen along the span, assuming that the sail sections at different span-wise positions are geometrically similar. This procedure introduces a small approximation, since strict geometrical similarity is not maintained along the span, but the effect is likely small.

The added mass forces are subsequently computed in the body-fixed coordinate system according to Eq. (16), before being transformed to the lift- and drag-directions, according to Eq. (17).

$$F_{AM,x} = (\lambda_{xx}\ddot{x} + \lambda_{xy}\ddot{y})\rho h b^2 \tag{16a}$$

$$F_{AM,y} = (\lambda_{yy}\ddot{y} + \lambda_{yx}\ddot{x})\rho h b^2 \tag{16b}$$

$$F_{AM,X} = \sin\beta F_{AM,y} - \cos\beta F_{AM,x} \tag{17a}$$

$$F_{AM,Y} = \sin\beta F_{AM,x} + \cos\beta F_{AM,y} \tag{17b}$$

3.1.5. Thrust and sideforce computation

To obtain the total instantaneous lift and drag of the sailplan, the different unsteady force components above are added to the steady lift and drag coefficients, and subsequently summed over the number of strips, as is shown in Eqs. (18a) and (18b) where k is the strip index, and n is the number of strips. The influence of the surge motion component is considered here through the instantaneous wind speed U_i', which is used here to compute the lift- and drag forces, thus, it could be said that the surge motion component is treated in a quasi-steady manner.

$$F_L = \sum_{i=0}^{n} 0.5a_i\rho U_i'^2\left(C_{L,S} + \frac{dC_l}{d\alpha}\alpha_{e,i}\right) + F_{AM,Y\,i} \tag{18a}$$

$$F_D = \sum_{i=0}^{n} 0.5a_i\rho U_i'^2\left(C_{D,S} + \Delta C_{D,p,i}\right) + F_{AM,X\,i} \tag{18b}$$

These can then be projected, in the heeled plane, with the apparent wind angle β to obtain the instantaneous thrust F_x and sideforce F_y as shown in Eqs. (19) and (20) below.

$$F_x = F_L\sin\beta - F_D\cos\beta \tag{19}$$

$$F_y = F_L\cos\beta + F_D\sin\beta \tag{20}$$

3.2. 2D CFD simulations

In this study, 2D CFD simulations were used for three purposes; to predict the steady (i.e. those that are generated by the airfoil in a constant free-stream and without any motion) lift ($C_{l,S}$) and drag coefficients ($C_{d,S}$), to which the unsteady correction of the model is applied; to predict unsteady time series of lift and drag for different

oscillatory motions, used for code verification and evaluation of model performance; and to compute the indicial response functions (IRFs) used to model the dynamic response. For these different applications, the same computational setup is used, with only time step and motion parameters changing. In the following sections, the computational setup will be described in detail, and results from a grid refinement study will be presented. To aid selection of suitable grid resolution, the discretisation uncertainty is estimated using the methods presented by Eça et al. (2019). For the steady cases, the uncertainty due to spatial discretisation was determined for steady values of the lift ($C_{l,S}$) and drag coefficients ($C_{d,S}$). No grid dependency study was done for the unsteady simulations; instead it is assumed that the grid resolution used for steady simulations is also sufficient for the unsteady simulations.

For the IRF computations the effect of temporal discretisation was evaluated by visual comparison of the indicial response function as computed with two different time step sequences.

3.2.1. Numerical scheme and physical modelling

The 2D simulations were performed in Siemens Simcenter STAR-CCM+ 2210-R8, using the segregated incompressible solver, with a SIMPLE pressure–velocity coupling scheme and a second-order convective scheme. The simulations for the grid dependency study were performed with the steady solver, and stopped when the normalised residuals had been reduced by five orders of magnitude.

The unsteady oscillatory simulations were performed using the implicit unsteady solver, with a second-order temporal scheme initialised by simulating 60 s without grid motion, using a time step of $\Delta t = 0.05$ s, so that the steady-state lift- and drag coefficients could be obtained. The grid motion was then ramped using a fifth-order polynomial function to ensure a smooth increase in grid velocity and acceleration, and a continuous jerk signal. During the unsteady phase, a time step of $\Delta t = T_p/200$ was used, where T_P is the oscillation period. A total of ten oscillation periods were simulated. In each time step, inner iterations were performed until the normalised residuals had been reduced by three orders of magnitude.

Turbulence was modelled using the one-equation Spalart–Allmaras model, following the results of the turbulence model sensitivity investigation presented by Persson et al. (2017). A low y^+ wall treatment was used, meaning that the boundary layer is resolved into the viscous sublayer. The grids were generated to ensure a y^+ value below 1.

3.2.2. Domain and boundary conditions

For the 2D simulations, a rectangular domain was used, extending 50 chord lengths upstream, above and below the section, and 100 chord lengths downstream of the section. The boundary conditions are shown in Fig. 10, with a velocity inlet condition used on the upstream and top/bottom boundaries, with velocity $U = 7.63$ m/s, $V = 0$ m/s. A pressure outlet condition is used on the downstream boundary with pressure $p = 0.0$ Pa. On the inlet and outlet boundaries, ambient turbulence is specified by turbulent viscosity ratio $R_T = 3$, as suggested by Spalart and Rumsey (2007). A no-slip smooth wall condition is used on the airfoil and sail surfaces.

3.2.3. Computational grid

A series of four unstructured hexahedral grids were generated. The far-field cell size ΔX was given in fractions of chord length c. For the 2D sail section, the chord length of the jib was used to define the far-field cell size, and zero-thickness baffle interfaces were used to represent the sail surfaces. In a hexahedral grid, refinements can be introduced by dividing the cell side in two. The cells on the airfoil and sail section surfaces were refined 7 times from the far-field cell size. The mast surface was refined 8 times, while an additional refinement of 10 times was introduced on the leading edge (LE) and trailing edge (TE). The cell size, refinements and other parameters are presented in Table 1.

While it is impossible to achieve true geometrical similarity in an unstructured grid, the surface growth rate, volume growth rate,
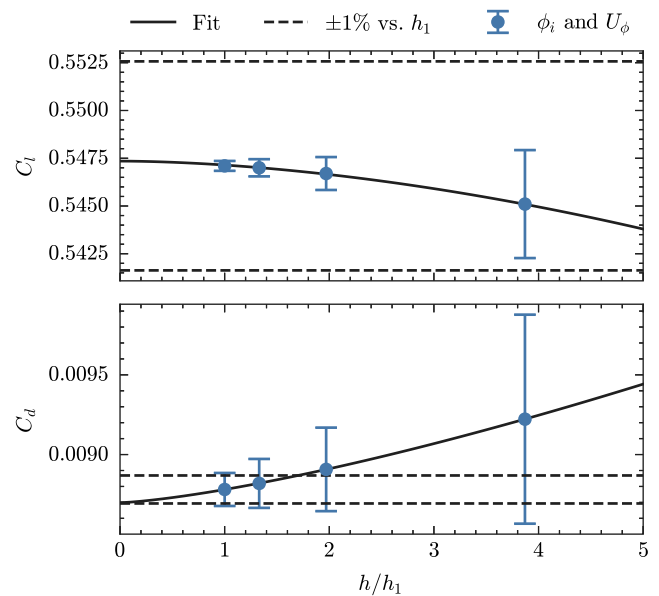

Fig. 8. Grid convergence and curve fit for steady uncertainty estimates, 2D NACA0006 airfoil.
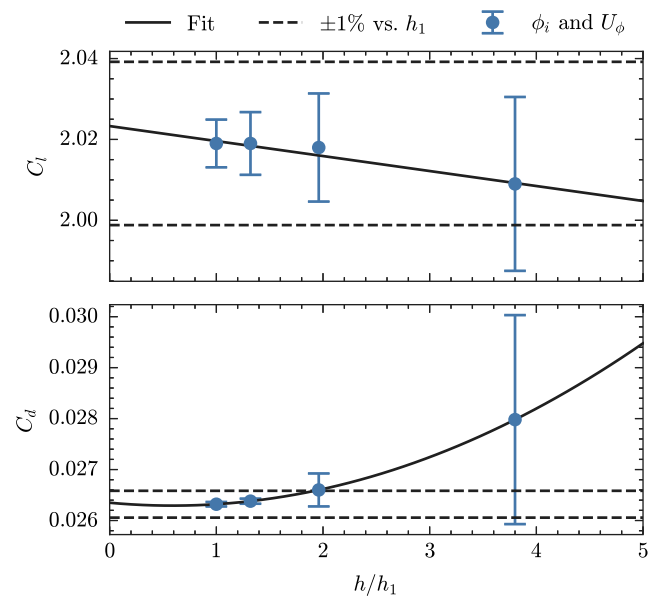

Fig. 9. Grid convergence and curve fit for steady uncertainty estimates, 2D sail section.

number of prism layers and y^+ were changed over the grid series maximise geometrical similarity. The first-cell height was chosen so that $y^+ = 1$ was obtained on the coarsest grid, and then successively refined over the grid series, reaching $y^+ = 0.25$ on the finest grid. The total thickness of the generated prism layer was set to the estimated turbulent boundary layer thickness for a flat plate. The number of prism layers was adapted in a similar way to the volume growth rate, ranging from 80 in G1 to 20 in G4. In Fig. 10, a far-field overview of the G4 grid is shown with the boundary conditions indicated. In Fig. 11, a detailed view of the NACA0006 G4 near-field grid is shown, while Fig. 12 shows a corresponding view of the 2D sail section grid.

The results of the grid dependence study and uncertainty estimate for the steady lift and drag coefficients of NACA0006 airfoil are shown in Table 2 and in Fig. 8, where the values for C_l and C_d obtained on the different grids are plotted against the relative refinement ratio h/h_1. The error bars indicate the respective discretisation uncertainties,

Table 1
Cell size, refinements and other grid parameters.

Grid	ΔX	Airfoil/sail cell size	Mast cell size	LE/TE cell size	Vol. growth rate	# prism layers	y^+
G1	$c/4$				16	80	0.25
G2	$c/3$	$\frac{\Delta X}{2^7}$	$\frac{\Delta X}{2^8}$	$\frac{\Delta X}{2^{10}}$	12	60	0.33
G3	$c/2$				8	40	0.5
G4	c				4	20	1

Table 2
Steady grid dependence and uncertainty estimate, 2D NACA0006 airfoil.

Grid	h_i	$C_{l,s}$ (−)	$C_{d,s}$ (−)	$U_{C_{l,s}}$ (%)	$U_{C_{d,s}}$ (%)
G1	1.00	0.5471	0.008781	0.05%	1.2%
G2	1.33	0.5470	0.008819	0.08%	1.7%
G3	1.97	0.5467	0.008907	0.16%	2.9%
G4	3.85	0.5451	0.009222	0.52%	7.1%

Table 3
Steady grid dependence and uncertainty estimate, 2D sail section.

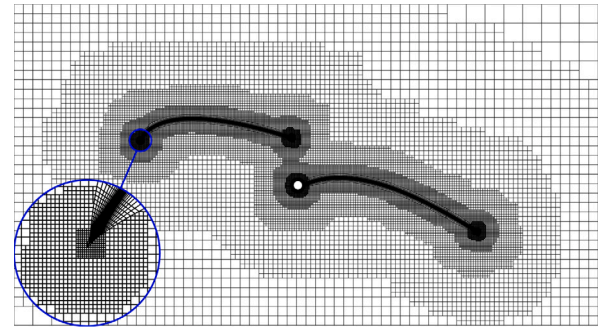| Grid	h_i	$C_{l,s}$ (−)	$C_{d,s}$ (−)	$U_{C_{l,s}}$ (%)	$U_{C_{d,s}}$ (%)
G1	1.00	2.019	0.02632	0.29%	0.17%
G2	1.32	2.019	0.02638	0.38%	0.19%
G3	1.96	2.018	0.02660	0.66%	1.2%
G4	3.80	2.009	0.02798	1.1%	7.3%

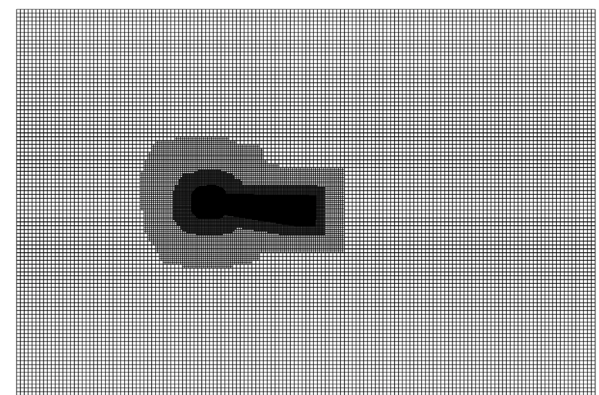**Fig. 12.** Near-field mesh detail, $G4$, 2D sail section.

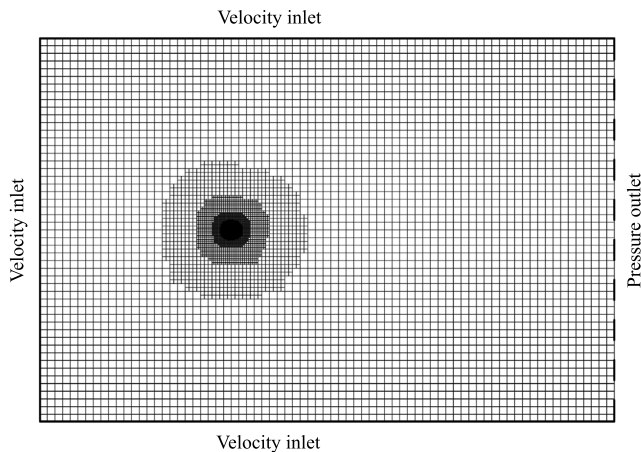**Fig. 13.** $G3$ far-field overview, with wake refinement.

Fig. 10. G4 far-field overview, without wake refinement. Applied far-field boundary conditions indicated.
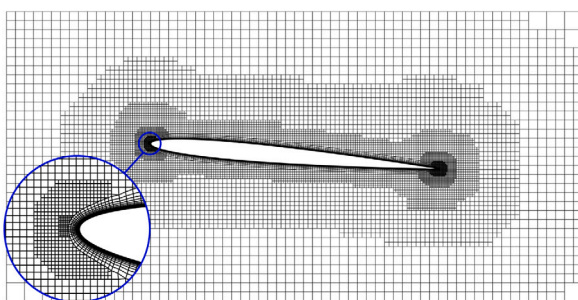

Fig. 11. Near-field mesh detail, $G4$, NACA0006 airfoil.

$U_{C_{l,s}}$ and $U_{C_{d,s}}$ The variation across the grid series was small (<0.5%) for the lift coefficient $C_{l,S}$, but somewhat larger (<4.5%) for the drag coefficient $C_{d,S}$. Similarly, the estimated uncertainties were very low for $C_{l,S}$, but somewhat larger for $C_{d,S}$. The results for the 2D sail section are shown in Table 3 and Fig. 9, the grid series variation was similar for the lift coefficient $C_{l,S}$, (<0.5%) but somewhat larger (≈6.3%) for

the drag coefficient $C_{d,S}$. The estimated uncertainties were in general slightly larger, but still remains at a low level.

Considering the results of the grid dependence study and uncertainty estimates presented above, grid resolution G3 was selected for use in subsequent simulations, for both the NACA0006 airfoil and the sail section. For the NACA0006 airfoil, this gives an uncertainty of 0.16% for $C_{l,S}$ and 2.9% for $C_{d,S}$. For the sail section, the estimated uncertainties were 0.66% for $C_{l,S}$ and 1.2% for $C_{d,S}$.

3.2.4. Wake refinement sensitivity

Since the circulatory unsteady effects are caused by vorticity shed in the wake, it is possible that additional refinement of the wake region could be required to predict the unsteady force variation. The sensitivity to wake refinement was investigated by generating an alternative grid, based on $G3$, for the 2D NACA0006 airfoil. An additional refinement was added to resolve the wake for 25 chord lengths behind the airfoil trailing edge, with the same cell size as that used on the airfoil surface. An unsteady oscillatory simulation was then performed using the alternative grid, at a reduced frequency $k = 0.1$, where the circulatory contribution can be expected to dominate the unsteady force variation, resulting in high sensitivity to the refinement of the unsteady wake. An overview of $G3$ with additional wake refinement is shown in Fig. 13.

A graphical comparison of the time histories is shown in Fig. 14 A quantitative comparison of the mean values and amplitudes of the unsteady force coefficients is shown in Table 4.
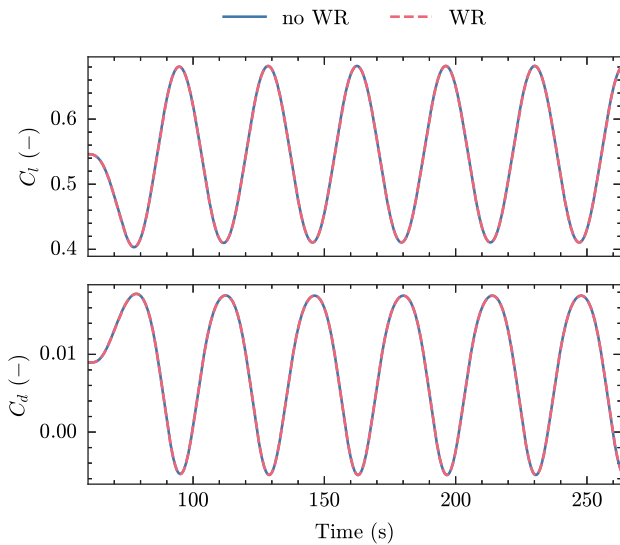
Fig. 14. Comparison of computed time histories, with and without wake refinement for the 2D NACA0006 airfoil.

Table 4
Effect of wake refinement on amplitude and mean value of force coefficients, NACA0006 airfoil.

	No WR ($G3$)	WR	Δ (%)
$\hat{C}_l$ (–)	0.1359	0.1359	0.02
$\bar{C}_l$ (–)	0.543	0.543	<0.01
$\hat{C}_d$ (–)	0.01156	0.01156	<0.01
$\bar{C}_d$ (–)	0.00770	0.00771	0.04

As can be seen from the results above, the difference in predicted force coefficients with and without wake refinement is minimal, and significantly smaller than the estimated discretisation uncertainty. This is true for all metrics evaluated. From this, it can be concluded that the unsteady wake does not need to be resolved in detail if the aim is to predict unsteady force coefficients. The fact that minimal dependence on wake refinement is seen indicates that the magnitude of the downwash induced by the unsteady wake remains the same, even if it is not resolved in detail.

3.3. Computing indicial response using CFD

In this work, IRFs generated with URANS CFD are utilised. In principle, IRFs can be computed for the 3D sail plan/wing, but in order to limit the computational effort of IRF generation, 2D simulations are used. While the Wagner function is an analytically derived indicial response function, based on thin airfoil theory, indicial response functions can also be derived from experimental results, or computed with CFD. This is a major advantage for sail modelling since the interaction effects between jib and mainsail make it difficult to derive an IRF analytically. For wing sail applications, which typically utilise a thick airfoil profile, indicial response functions computed with CFD can also capture the viscous effects related to airfoil thickness.

In order to evaluate the influence of time-step choice, two different time-step sequences have been tested. These sequences are shown in Fig. 15.

A comparison of the generated IRFs for the NACA0006 section, with the two different time-step sequences, is shown in Fig. 16. At the scale presented here, no significant differences can be seen. Some minor differences can however be seen at small values of non-dimensional time, $s < 0.1$.

In Fig. 17, a comparison between the Jones approximation of the Wagner function and the CFD computed IRF for the NACA0006 airfoil
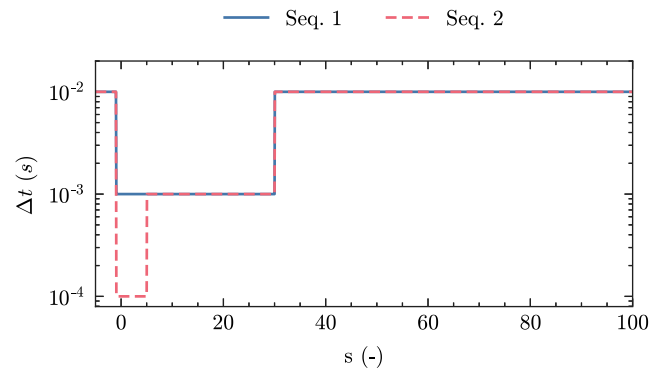

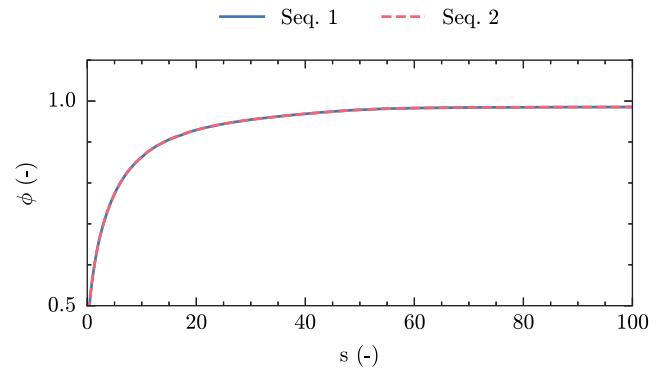**Fig. 15.** Time step sequences used for IRF computations.

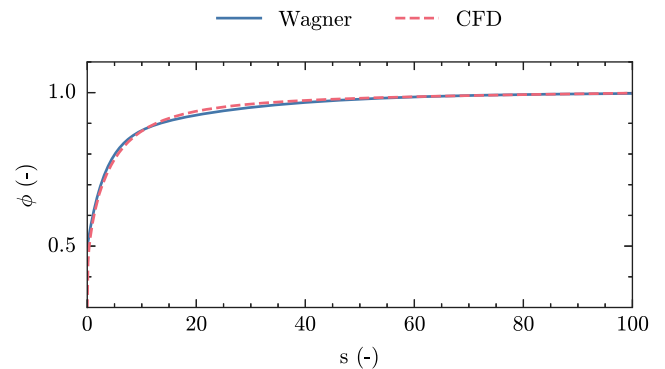**Fig. 16.** CFD computed IRF; time step sequence sensitivity.

Fig. 17. Comparison between Jones approximation of the Wagner function and the CFD IRF for a NACA0006 airfoil.

is shown. Minor differences can be seen over a wide range of s-values, and can likely be attributed to the effects of airfoil thickness and fluid viscosity, since these effects are included in the CFD IRF while the Wagner function is based on thin-airfoil theory, and thus ignores these effects.

3.3.1. 3D CFD simulations

The 3D simulations were also performed using Siemens Simcenter STAR-CCM+ 2210-R8, and using the same solvers, discretisation schemes and physics models as those used for the 2D simulations (see Section 3.2). The domain configuration, boundary conditions, and general simulation setup are taken from Persson et al. (2017), but
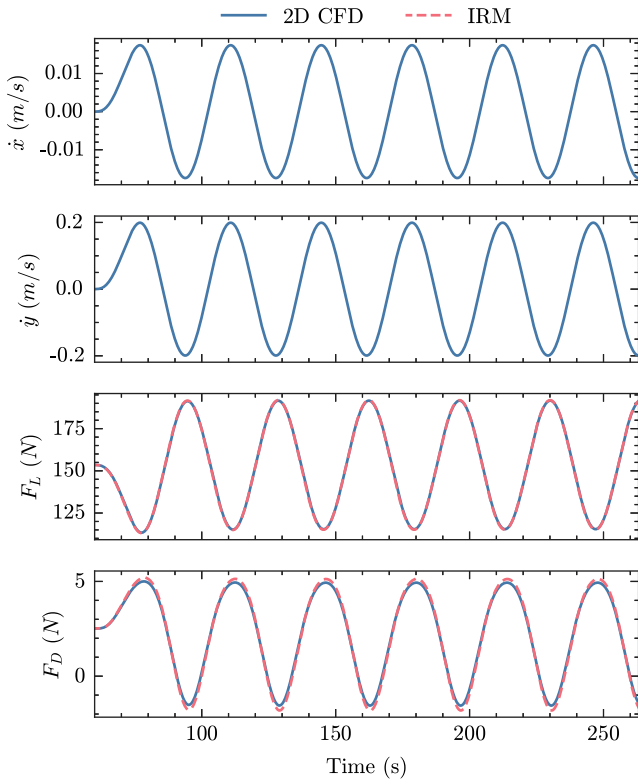
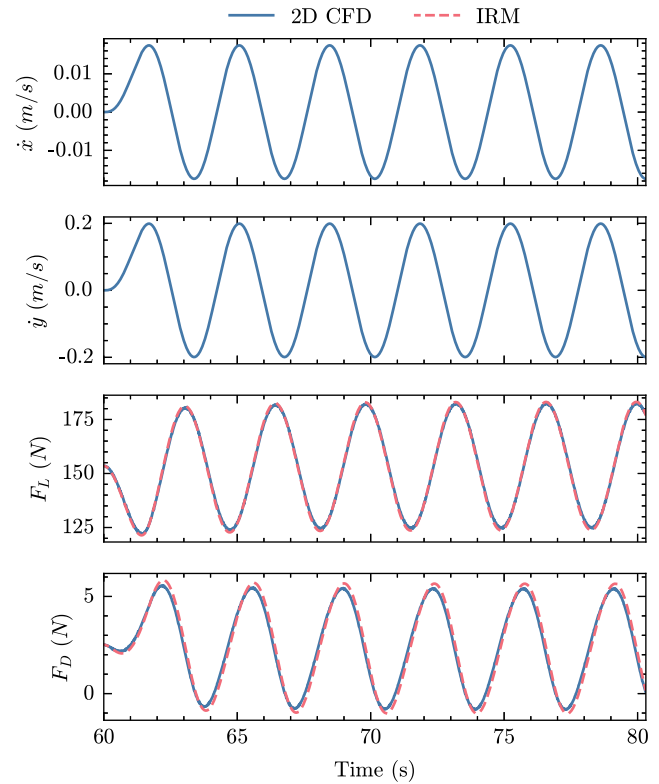**Fig. 18.** NACA0006 airfoil, plunge motion; $k = 0.1$.

Fig. 19. NACA0006 airfoil, plunge motion; $k = 1$.

some simplifications and adaptations have been made, considering the purpose of the current study. In Persson et al. (2017), the aim was to validate CFD prediction of steady and unsteady aerodynamic forces against wind tunnel test data, which required additional steps to replicate wind tunnel test conditions in detail. Since the aim of the current study is to develop low-order modelling strategies, detailed replication of wind tunnel test conditions is not required. This allows the removal of the additional boundary surfaces used in Persson et al. (2017) to represent the roof and floor of the wind tunnel, leading to a substantial reduction in grid size and the elimination of two overset interfaces, which together significantly reduces computational effort. Additionally, since the aim is to predict unsteady force variations on a full scale sailplan, the 3D simulations are performed at full scale Reynolds number, in contrast to Persson et al. (2017), where model scale simulations were performed.

For the 3D simulations, a coarser grid (equivalent to $G4$ in 2D) had to be used to conserve computational resources. In order to extract the input data required for the IRM model, additional probe points and local, body-fixed coordinate systems have been introduced. These are located at the strip area centroid height d_w allowing the velocity and acceleration to be extracted for each strip, and at each time-step, as described in Section 3.1.1.

4. Results

While the aim of this paper is to model the unsteady aerodynamic forces on a pitching 3D sailplan, the model has been evaluated on two different 2D geometries, a NACA0006 airfoil and a 2D sail section, for a number of different motions. This has two purposes; firstly, to verify that the model code implemented can accurately predict the unsteady lift coefficient on a case which is as close to ideal potential flow as practically possible; secondly, to provide an indication of which phenomena contribute to potential modelling errors, by systematically increasing the complexity of the modelled cases.

4.1. 2D pure plunge motion

A pure plunge motion case was evaluated for both geometries, with the airfoil set at a mean angle-of-attack α_m in a steady freestream velocity U, being subjected to a motion perpendicular to the freestream, in the form of a harmonic oscillation with plunge velocity amplitude $\hat{y}$. The motion parameters are shown in Table 5. The 2D NACA0006 airfoil constitutes a simple verification case, where both geometry and motion characteristics are similar to those seen in typical applications for IRM models, falling well within the underlying assumptions. For this case, good agreement can be expected, allowing the current IRM implementation to be verified. The 2D cases will be evaluated at two different reduced frequencies; at $k = 0.1$, the non-circulatory (added mass) forces are small, and circulatory contributions can be assumed to dominate the solution (Leishman, 2006). At higher reduced frequencies, in this case $k = 1$, the non-circulatory forces instead dominate. As can be seen from Figs. 18 to 19, the IRM model predictions of lift coefficient show excellent agreement with CFD, with a comparison error of $<0.1\%$ for the mean values and between 0.7% and 2% for the amplitude. For drag, the prediction of mean values is good, with comparison errors between 0.3% and 0.6%; however, larger discrepancies are seen for amplitude (6.8%–7.2%), which is slightly over-predicted by the IRM model. The comparison error increases with slightly with increased reduced frequency.

The 2D sail section introduces some of the additional complexity described in Section 3.1; interaction between the two elements of the sailplan, and the added mass cross-coupling. The inclusion of this case allows these effects to be separated from those introduced by the additional surge motion that occurs in the combined motion test cases, giving some indication as to the source of potential modelling errors. A comparison of the predicted time histories for lift- and drag forces are shown in Figs. 20 to 21. For $k = 0.1$, the mean value of lift is over-predicted by 0.8%, while the amplitude is under-predicted by 2.2%. For the drag force, the mean value is under-predicted by 18%, and the

Table 5

Parameters of the pure plunge motion cases, NACA0006 and 2D sail section.

Case	c (m)	U (m s^{-1})	α_m (°)	$\hat{y}$ (m s^{-1})	k (–)
NACA0006	8.226	7.63	5	0.2	0.1, 1.0
2D sail section	8.226	7.63	16	0.45	0.1, 1.0

Table 6

Parameters of the oblique motion case.

Case	c (m)	U (m s^{-1})	α_m (°)	$\hat{y}$ (m s^{-1})	k (–)
NACA0006	8.226	7.63	5	0.2	0.1, 1.0

Table 7

Parameters of the chordwise motion case.

Case	c (m)	U (m s^{-1})	α_m (°)	$\hat{x}$ (m s^{-1})	k (–)
2D sail section	8.226	7.63	16	0.45	0.1, 1.0

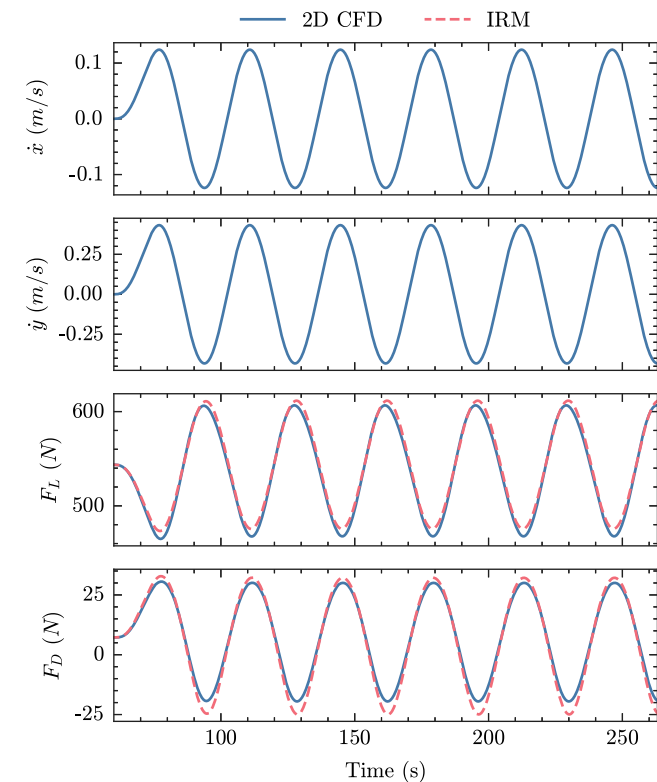**Fig. 20.** 2D sail section, plunge motion; $k = 0.1$.

Fig. 21. 2D sail section, plunge motion; $k = 1$.

amplitude is over-predicted by 15%. The results for the higher reduced frequency, $k = 1$, show similar results for lift but with smaller errors for the mean value (0.25%) and larger errors for amplitude (6.5%). For drag, the mean value is under-predicted by 33% while the amplitude is over-predicted by 19%. Phase is predicted well for lift and drag at low k, but some discrepancy can be seen at high k, particularly for drag.

4.2. 2D oblique motion

An oblique motion case was simulated for the 2D NACA0006 airfoil, in which the oscillatory motion was applied at a 45° angle to the freestream direction. This case isolates the effects of combined motion from the interaction effects associated with the jib-mainsail section. Furthermore, since the oblique motion occurs at a 45° angle, the surge and plunge motion amplitudes will be similar, providing an intermediate case between the pure plunge case and the chordwise motion case. This allows the relative importance of the surge motion component
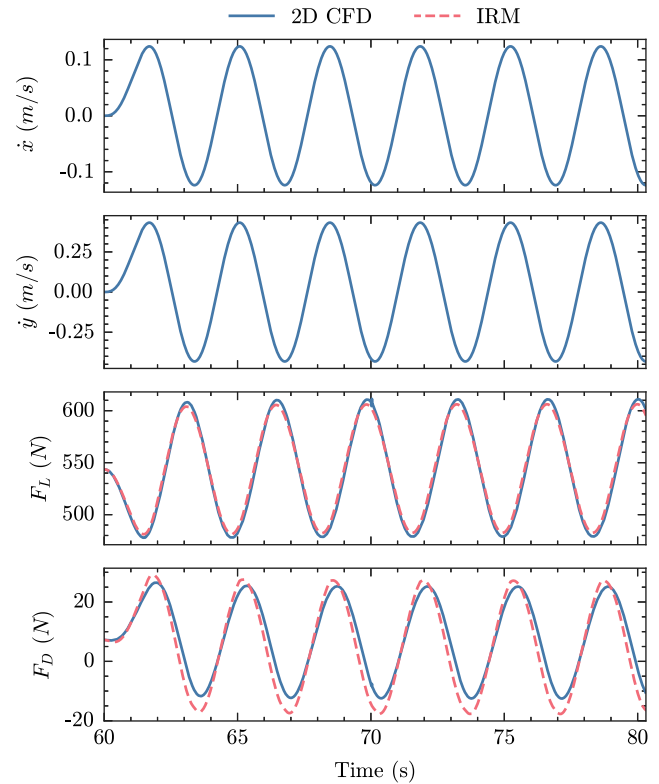
to be assessed, which is relevant since this is only modelled using a quasi-steady assumption. The high-frequency motion also allows the influence of added mass in surge to be assessed, without the cross-coupling, off-diagonal components of the sail section. The motion parameters for this case is shown in Table 6. Figs. 22 to 23 show a comparison of the predicted time histories for lift- and drag forces.

For $k = 0.1$, the mean value of the lift is predicted well, with a comparison error <0.1%, while the amplitude is under-predicted by 0.53%. The mean drag is over-predicted by 0.49%, while the amplitude is over-predicted by 5.63%.

Also, for $k = 1$, the lift mean value is well predicted, with a comparison error of 0.5%. However, the lift amplitude is slightly under-predicted, by 3.1%. The mean value of drag was over-predicted by 0.7%, but the amplitude is instead under-predicted by 1.42%.

4.3. 2D chordwise motion

As is described in Section 3.1.1, the 3D pitching motion experienced by a vessel sailing upwind in waves is here approximated by a chordwise linear translation. The motion parameters are shown in Table 7. This case replicates the simplified motion in a 2D case, eliminating the complication of 3D effects, such as finite span effects and the variation in reduced frequency and motion amplitude along the span. This allows the validity of the motion decomposition procedure and added mass modelling to be investigated, which are key considerations for the sail section, as described in Section 3.1. Figs. 24 to 25 show a comparison of the predicted lift- and drag forces.

For $k = 0.1$, the mean values are again predicted well, with a comparison error of 0.11% for lift and 0.72% for drag. However, for amplitude the errors are larger, at 9.2% for lift and −5.2% for drag.

For $k = 1$, the mean value for lift shows good agreement, with a comparison error of 0.52%. However, for drag, the mean value shows worse agreement, with a comparison error of 7.3%. The lift amplitude is over-predicted with 33% while the drag amplitude is under-predicted
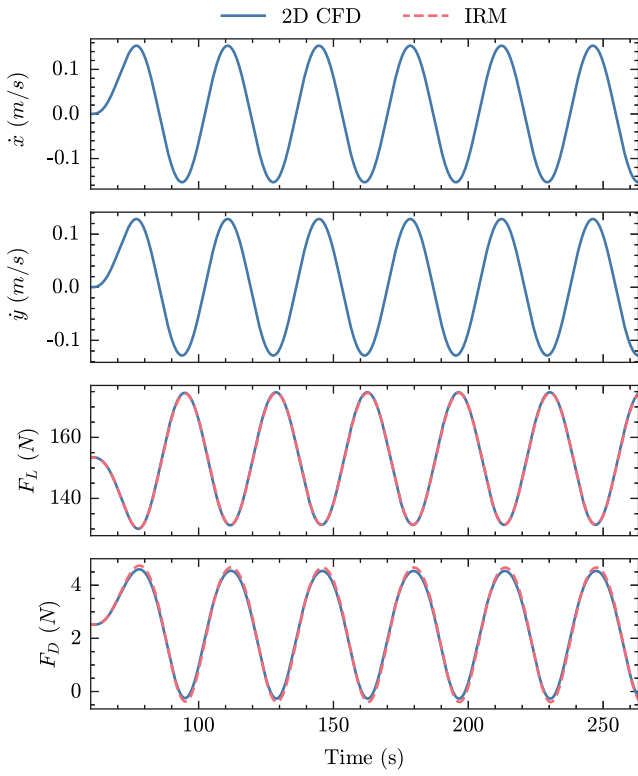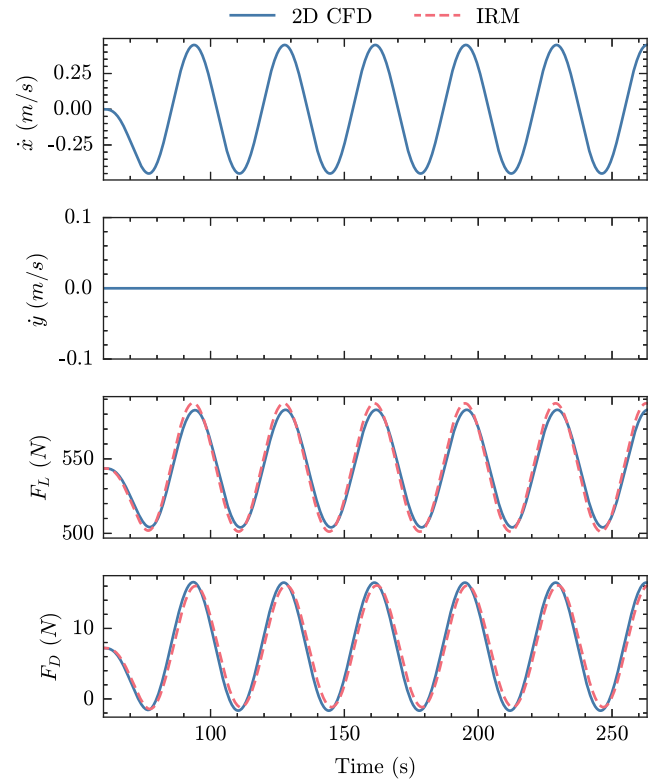
Fig. 22. NACA0006, oblique motion; *k* = 0.1.

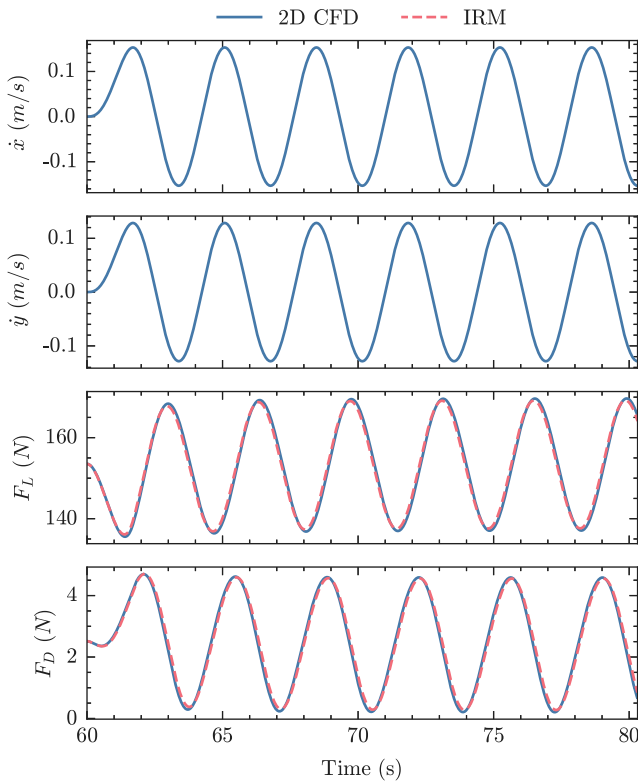**Fig. 24.** Jib-mainsail, chordwise motion; *k* = 0.1.

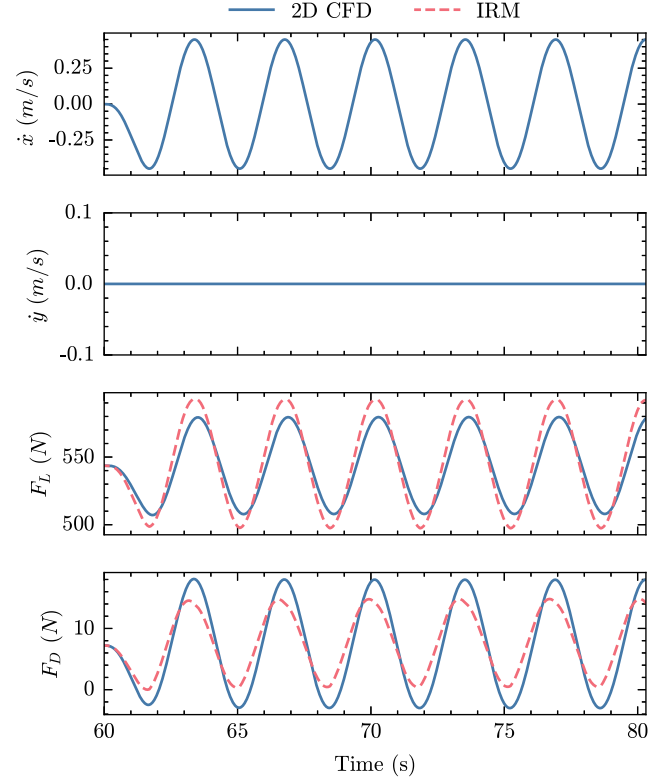**Fig. 23.** NACA0006, oblique motion; *k* = 1.
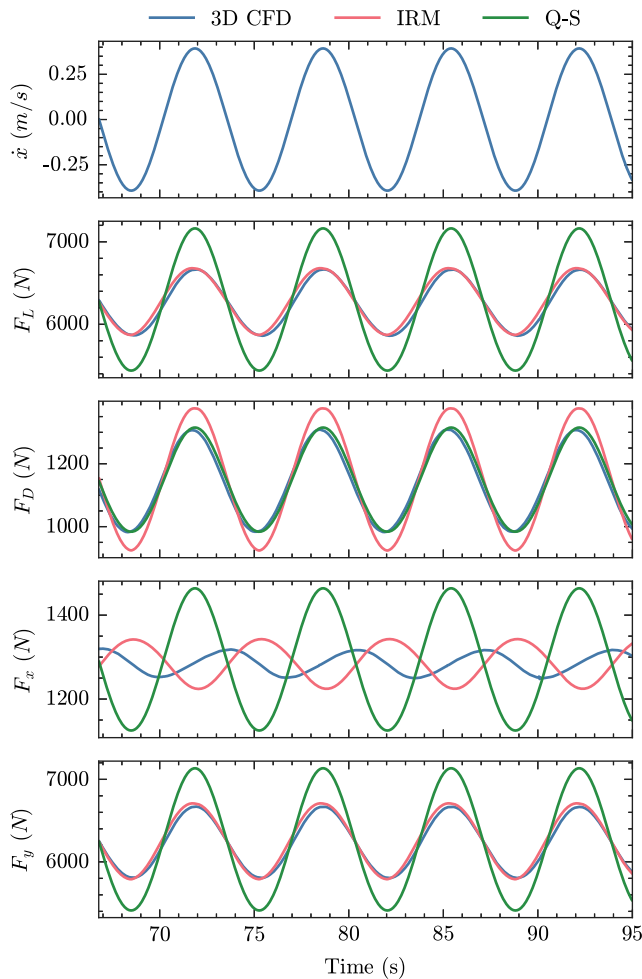

Fig. 25. Jib-mainsail, chordwise motion; *k* = 1.

Fig. 26. 3D sail plan, pitch motion; $k = 0.5$.

Table 8
Parameters of the 3D pitch motion case.

Case	A (m²)	U (m s^{-1})	β_m (°)	$\hat{\theta}$ (°)	k at z_{CE} (–)
3D sail plan	109.3	7.63	22	1.3	0.5

the maximum longitudinal acceleration $\ddot{x}$ is approximately 0.24 m s^{-2}. This can be compared to the corresponding values for the uppermost strip, with $k \approx 0.15$, $\alpha' \approx 2.6°$ and $\ddot{x} \approx 0.78$ m s^{-2}, revealing that while the reduced frequency is significantly lower for the topmost strip, the unsteady angle of attack variation and accelerations are significantly larger.

In Fig. 26, a comparison of the predictions of the stripwise IRM with 3D URANS CFD is shown, with results from the typical quasi-steady model included for reference. For this case, thrust F_x and sideforce F_y have also been computed according to Section 3.1.5, as these are the key variables of interest for performance prediction. In general, the 3D lift force F_L is very well predicted, with comparison errors for mean value of 0.48% and for the amplitude of 0.5%. For the drag force F_D, the mean value is also well predicted, with an error of 0.53%. However, the predictions of drag amplitude show large errors, with an over-prediction of 38%. There is also a small phase shift between the URANS CFD and IRM prediction, but this has not been quantified.

For the thrust F_x, the mean value is well predicted, with an error of 0.4%. However, very large discrepancies can be seen for the amplitude, which is over-predicted by 69%. The sideforce F_y is relatively well predicted, with comparison errors of 0.48% for the mean value and 7% for amplitude.

The Q-S model performs equally well as the IRM model for predicting mean values, with comparison errors <1%, but grossly over-predicts lift amplitude, leading to misprediction of thrust and sideforce amplitude. However, drag amplitude is surprisingly well predicted, with a comparison error of 1.5%.

5. Discussion

In this study, an IRM model for unsteady upwind sail aerodynamics has been implemented and the predictions have been compared to results from URANS CFD simulations. For a NACA0006 airfoil in pure plunge, the predictions agree well, verifying that the method has been correctly implemented. For the 2D sail section, subjected to pure plunge motion, the agreement is slightly worse, indicating that some aspect of the sail case is not fully captured by the current model. For example, the unsteady interaction between the sails may not be properly described by the IRF, or there may be a change in lift curve slope due to viscous effects during the motion. It can also be seen that the comparison error increases slightly with increasing reduced frequency k, which could indicate that the added mass modelling contributes to the modelling error.

For the NACA0006 airfoil, subjected to oblique motion, the agreement is good. This indicates that the assumptions behind the motion decomposition procedure works well, and that the quasi-steady surge model and added mass treatment works well for this intermediate combined motion case where no added mass cross-coupling effects are present. For the 2D sail section, subjected to chordwise motion, the results are relatively good for low k, but deteriorate significantly at high k. This could indicate that the motion decomposition and quasi-steady surge model works well for this case, but that the added mass model fails to capture the added mass forces. Notably, this is the only case where added mass cross-coupling is expected to be significant.

For the 3D case, the IRM model predicts the mean value and amplitude of lift well, especially compared to the Q-S model which grossly over-predicts the lift amplitude. The relative lift amplitude predicted with URANS CFD and the IRM model is approximately 6.5% which agrees well with the findings of Gerhardt et al. (2011). Also the mean

31%, showing worse agreement than for the lower reduced frequency case.

4.4. 3D pitch motion

In order to evaluate the model performance on a realistic case, representative of the intended final usage of the model, a 3D test case has also been simulated. The motion frequency and amplitude was extracted from a 6DOF CFD-VPP simulation of the SYRF14 yacht (as described in detail in Persson et al. (2020)), sailing upwind in a true wind speed of 8 knots, in quartering waves with a wave height of 0.8 m and wave period of 5.1 s. This results in an average boat speed of approximately 7.9 knots, and an encounter period of approximately 6.8 s. A quasi-steady coefficient-based sail model was used to model the sail forces. The motion extracted from the simulation is six degree-of-freedom, which was then simplified to a one degree-of-freedom pitch motion with the same pitch period and amplitude as that seen in the CFD-VPP simulation. The motion parameters used here are shown in Table 8. The pitch motion is assumed to occur around a transverse axis through the vessel centre of gravity, which together with the significant span (18.7 m) of the sail plan, means that the unsteady angle of attack α', unsteady wind velocity U' and the accelerations will vary greatly along the span, with amplitudes increasing with height. Furthermore, the sailplan has a tapered planform, with chord length decreasing with height, and thus, reduced frequency k will also decrease with height. For the bottom strip, the reduced frequency k is approximately 0.67, the maximum unsteady angle of attack α' is approximately 0.7°, and

value of drag is well predicted, but the amplitude of drag is significantly over-predicted by the IRM model, while the Q-S model, unexpectedly predicts mean value, amplitude and phase of drag very well. Both IRM and Q-S models predict mean value of thrust well, while the IRM model predicts amplitude of thrust better. However, both models mispredict the phase of thrust, compared to URANS CFD. For the sideforce, the IRM model predicts the mean value, amplitude and phase well, while the Q-S model again (as a consequence of the lift amplitude error) grossly over-predicts amplitude.

The difficulty in predicting unsteady thrust for upwind sailing was unexpected, but can be explained by how thrust is computed, see Eq. (19). When sailing upwind, the apparent wind angle β will be small; subsequently, the value of $\sin\beta$ will be small, while the value of $\cos\beta$ will be close to unity. Combined with the lift-to-drag ratio, which here is between 5 and 6 it becomes apparent that, when computing thrust, a large part ($\cos\beta$) of a small force (drag) is subtracted from a small part ($\sin\beta$) of a large force (lift). This infers that the sum will be small, and that the result will be very sensitive to variations in the phase and amplitude of the lift and drag forces. As far as the authors are aware, this has not been concluded in previously published research.

For upwind performance prediction, it can be argued that the accurate prediction of thrust mean value is more important than thrust amplitude. Since the yacht's inertia and moment to trim is large, the unsteady variation of thrust will most likely result in only small accelerations and changes in trim. However, for sideforce, accurate prediction of both mean value and amplitude is believed to be important. The unsteady variation of sideforce will primarily affect the heel angle of the yacht. Considering the large moment arm between sailplan and keel, it seems plausible that the unsteady variation in sideforce could bring about a change in heel during a wave encounter. The heel of the yacht subsequently contributes to many effects that are of importance to velocity prediction, such as added resistance due to heel, loss of effective draft of the keel and by shifting the centre of effort of the sails laterally, altering the yaw moment balance of the vessel and requiring the rudder angle to be adjusted.

The proposed model has important limitations, some which could impact the model performance within the scope of this paper, and some which limit the applicability of the model to points of sail other than upwind. A fundamental assumption inherent to the Indicial Response Method is that the relation between angle-of-attack and lift coefficient is linear, which limits the method to attached flow conditions only. This can be problematic for reaching or downwind sailing, where the sails are often sheeted to achieve maximum lift, or even beyond this point, into a fully-stalled condition. Furthermore, the wing sails that are currently used for ship propulsion will most likely be operated at high angles-of-attack, close to the point of stalling, in search of maximum thrust force, and thus, the applicability of the model to such cases must also be investigated further.

When using the 2D CFD-computed Indicial Response Functions to model the unsteady aerodynamic response of the 3D sail plan, the following simplifications are introduced; each strip is treated separately, and no interaction effects between the strips are considered; the unsteady velocities and accelerations are considered to be constant across the height of the strip; and any unsteady finite span effects, such as 3D loss-of-lift and induced resistance, are neglected. While the importance of the two first effects could be estimated by increasing the number of strips used to discretise the sailplan, the importance of finite span effects are harder to estimate. As is presented by Reissner and Stevens (1947), the magnitude of the unsteady finite span effects on lift force depend on wing planform, aspect ratio and the reduced frequency k. For an elliptic wing of aspect ratio 6, subjected to uniform translation and pitching, Reissner and Stevens (1947) showed that the finite span effects are small at the rather high reduced frequencies considered here.

In this study, the discretisation of the 3D sail plan is rather coarse, and while initial studies showed only slight sensitivity to the number of strips used in the discretisation, other discretisation strategies should

be explored, for example using a variable strip height h over the span of the sail. Moreover, while a masthead sail plan is used in this study, the model can also be used for fractional sail plans. This requires that an additional indicial response function is generated for the mainsail-only sections above the forestay fitting.

A limitation of this study is the exclusive reliance on Computational Fluid Dynamics (CFD) simulations, without any validation against experimental results. While validation against experimental results is an important method to support the development of numerical models, the difficulty involved in obtaining unsteady experimental data means that only limited experimental data is available for sails. As far as the authors are aware, two data sets are available, but these are not readily usable for validation in this study; Gerhardt et al. (2008) measured pressure distributions, but not any forces; and the results of Fossati and Muggiasca (2011) are affected by details of the experimental setup (as discussed in Persson et al., 2017) which would be very difficult to account for in the IRM model. When discussing this limitation it is important to consider the aim of this study; to develop a low-order model which predicts unsteady force variation on full scale sails. For this purpose, full-scale 3D URANS CFD can be considered state-of-the-art, and therefore it seems reasonable to use this as a reference when developing a low-order model. To mitigate the effect this limitation, a number of steps have been taken to ensure that high-quality CFD solutions are used, with high cell-count, refined grids and small time-steps, along with strict criteria for iterative convergence. For the 2D simulations, the discretisation uncertainty has been investigated using best-practice methods (Eça et al., 2019) and shown to be low.

A unique aspect of sails, compared to the wings used in the aeronautical sector, is that they are made of relatively soft textile materials, and thus subject to change of shape during normal operation. For this reason, Fluid-Structure Interaction effects are sometimes modelled in sail simulations, but for this study, all such effects are neglected, and the sails are considered to be stiff. It is possible that FSI effects could alter the unsteady force variation in some scenarios, for example if the sails back-wind during the vessel motion. However, it is reasonable to expect the crew to manoeuvre the vessel, and trim the sails, in such a way to avoid this since back-winding would result in a significant loss of thrust. These effects are therefore considered to be of relatively minor importance for the purposes of unsteady performance prediction, but could be very important for detailed simulation of manoeuvres such as tacking.

6. Conclusions

In this paper, a model for unsteady upwind sail aerodynamics has been proposed. The model is based on the Indicial Response Method, a contemporary model often utilised for fixed wing aeroelasticity and helicopter rotor aerodynamics applications. Several important aspects that distinguish sail aerodynamics from the typical applications of IRM models have been identified, and expansions have been suggested to include these effects.

The model implementation has been verified using a simple test case, which is well within the fundamental assumptions of the theory, showing good agreement for low- and high values of reduced frequency. By examining the model's performance for cases with increasing levels of complexity, an indication of the limitations of the model have been obtained. In general, the model performance deteriorates with increasing reduced frequency k and increasing unsteady wind speed amplitude U'. This could indicate that the modelling error is mostly related to added mass and the unsteady effects caused by the surge motion component, so these aspects should be prioritised for further development.

In comparison to the commonly used quasi-steady approximation, the proposed unsteady model significantly improves the prediction of the amplitude for thrust and sideforce. This improved accuracy is believed to be important for performance prediction on timescales

shorter than the wave period. However, the proposed model fails to predict the amplitude of drag force. In contrast, the Q-S model shows surprisingly good agreement for drag. The reason for this should be investigated further, to obtain a better understanding of the unsteady drag, supporting the development of an improved drag model. A possible short-term solution to obtain a better overall force modelling for unsteady performance prediction could be to combine the unsteady lift force model proposed here, with the use of a Q-S approximation to predict drag. This could result in further improvement of the prediction of thrust amplitude and phase.

While some existing methods, for example unsteady VLM codes, can model additional phenomena, and likely provide an improved force prediction compared to the model presented here, these require detailed knowledge of the sail geometry. Early in a design process, when the hull design and appendage configurations are defined, such detailed knowledge of the sail shape are not yet available. The authors believe that the proposed model can allow the effects of unsteady sail forces to be considered in an approximate manner at this early design stage, based on a sail plan drawing and an approximate sail section.

CRediT authorship contribution statement

Adam Persson: Conceptualization, Methodology, Software, Validation, Writing – original draft. **Lars Larsson:** Supervision, Writing – review & editing. **Christian Finnsgård:** Supervision, Writing – review & editing, Funding acquisition.

Declaration of competing interest

The authors declare that they have no known competing financial interests or personal relationships that could have appeared to influence the work reported in this paper.

Data availability

The authors do not have permission to share data.

Acknowledgements

References

Augier, B., Bot, P., Hauville, F., Durand, M., 2012. Experimental validation of unsteady models for fluid structure interaction: Application to yacht sails and rigs. J. Wind Eng. Ind. Aerodyn. 101, 53–66. http://dx.doi.org/10.1016/j.jweia.2011.11.006.

Augier, B., Bot, P., Hauville, F., Durand, M., 2013. Dynamic behaviour of a flexible yacht sail plan. Ocean Eng. 66, 32–43. http://dx.doi.org/10.1016/j.oceaneng.2013.03.017.

Augier, B., Hauville, F., Bot, P., Aubin, N., Durand, M., 2014. Numerical study of a flexible sail plan submitted to pitching: Hysteresis phenomenon and effect of rig adjustments. Ocean Eng. 90, 119–128. http://dx.doi.org/10.1016/j.oceaneng.2014.06.040.

Azcueta, R., 2002. Ranse simulations for sailing Yachts including dynamic sinkage & trim and unsteady motions in waves. In: The Proceedings of the 1st High Performance Yacht Design Conference. Auckland, New Zealand.

Beckers, D., Eldredge, J.D., 2022. Planar potential flow on Cartesian grids. J. Fluid Mech. 941, http://dx.doi.org/10.1017/jfm.2022.238.

Bisplinghoff, R.L., Ashley, H., Halfman, R.L., 1983. Aeroelasticity. Dover Publications.

Böhm, C., Graf, K., 2010. Coupling of RANSE CFD with VPP methods: from the numerical tank to virtual BoatTesting. In: The Proceedings of the 2nd International Conference on Innovation in High Performance Sailing Yachts. Lorient, France.

Brennen, C.E., 1982. A Review of Added Mass and Fluid Inertial Forces. Technical Report CR 82.010, Naval Civil Engineering Laboratory, Port Hueneme, California, USA.

Day, S., Letizia, L., Stuart, A., 2002. VPP VS PPP: Challenges in the time-domain prediction of sailing Yacht performance. In: High Performance Yacht Design Conference. Auckland, New Zealand.

Eça, L., Vaz, G., Toxopeus, S.L., Hoekstra, M., 2019. Numerical errors in unsteady flow simulations. J. Verif. Valid. Uncertain. Quantif. 4 (2), 021001-1–021001-10. http://dx.doi.org/10.1115/1.4043975.

Fossati, F., Muggiasca, S., 2010. Numerical modelling of sail aerodynamic behavior in dynamic conditions. In: The Proceedings of the 2nd International Conference on Innovation in High Performance Sailing Yachts 2010. Lorient, France, http://dx.doi.org/10.3940/rina.innovsail.2010.02.

Fossati, F., Muggiasca, S., 2011. Experimental investigation of sail aerodynamic behavior in dynamic conditions. J. Sailboat Technol. 2011 (02).

Fossati, F., Muggiasca, S., Martina, F., 2008. Experimental database of sails performance and flying shapes in upwind conditions. In: The Proceedings of the International Conference on Innovation in High Performance Sailing Yachts. Lorient, France, p. 16.

Gerhardt, F.C., Flay, R.G.J., Richards, P., 2008. Unsteady aerodynamic phenomena associated with sailing upwind in waves. In: The Proceedings of the 3rd High Performance Yacht Design Conference. Auckland, New Zealand, pp. 148–157.

Gerhardt, F.C., Flay, R.G.J., Richards, P., 2011. Unsteady aerodynamics of two interacting yacht sails in two-dimensional potential flow. J. Fluid Mech. 668, 551–581. http://dx.doi.org/10.1017/S0022112010004842.

Ghoreyshi, M., Jirásek, A., Cummings, R.M., 2012. Computational investigation into the use of response functions for aerodynamic-load modeling. AIAA J. 50 (6), 1314–1327. http://dx.doi.org/10.2514/1.J051428.

Glauert, H., 1930. The force and moment on an oscillating aerofoil. In: Gilles, A., Hopf, L., v. Kármán, T. (Eds.), Vorträge Aus Dem Gebiete Der Aerodynamik Und Verwandter Gebiete: Aachen 1929. Springer Berlin Heidelberg, Berlin, Heidelberg, pp. 88–95. http://dx.doi.org/10.1007/978-3-662-33791-2_16.

Harris, D.H., 2005. Time domain simulation of a Yacht sailing upwind in waves. In: The Proceedings of the 17th Chesapeake Sailing Yacht Symposium. Annapolis, Maryland, USA, pp. 13–32.

Horel, B., Durand, M., 2019. Application of system-based modelling and simplified-FSI to a foiling open 60 monohull. J. Sail. Technol. 4 (01), 114–141. http://dx.doi.org/10.5957/jst.2019.4.1.114.

Kerdraon, P., Horel, B., Bot, P., Letourneur, A., Le Touzé, D., 2020. Development of a 6-DOF dynamic velocity prediction program for offshore racing yachts. Ocean Eng. 212, http://dx.doi.org/10.1016/j.oceaneng.2020.107668.

Larsson, L., 1990. Scientific methods in Yacht design. Annu. Rev. Fluid Mech. 22, 349–385.

Leishman, J.G., 1988. Two-dimensional model for airfoil unsteady drag below stall. J. Aircr. 25 (7), 665–666. http://dx.doi.org/10.2514/3.45639.

Leishman, J.G., 1993. Indicial lift approximations for two-dimensional subsonic flow as obtained from oscillatory measurements. J. Aircr. 30 (3), 340–351. http://dx.doi.org/10.2514/3.46340.

Leishman, J., 2006. Principles of Helicopter Aerodynamics. In: Cambridge Aerospace Series, Cambridge University Press.

Lesieutre, D., Reisenthel, P., Dillenius, M., 1994. A practical approach for calculating aerodynamic indicial functions with a Navier-Stokes solver. In: 32nd Aerospace Sciences Meeting and Exhibit. American Institute of Aeronautics and Astronautics, Reno, Nevada, USA, pp. 1–11. http://dx.doi.org/10.2514/6.1994-59.

Levin, R.L., Larsson, L., 2017. Sailing yacht performance prediction based on coupled CFD and rigid body dynamics in 6 degrees of freedom. Ocean Eng. 144, 362–373. http://dx.doi.org/10.1016/j.oceaneng.2017.09.052.

Mccroskey, W., Goorjian, P., 1983. Interactions of airfoils with gusts and concentrated vortices in unsteady transonic flow. In: 16th Fluid and Plasmadynamics Conference. American Institute of Aeronautics and Astronautics, Danvers, Massachusetts, USA, pp. 1–22. http://dx.doi.org/10.2514/6.1983-1691.

ORC, 2023. ORC VPP documentation.

Ōtomo, S., Henne, S., Mulleners, K., Ramesh, K., Viola, I.M., 2021. Unsteady lift on a high-amplitude pitching aerofoil. Exp. Fluids 62 (1), 6. http://dx.doi.org/10.1007/s00348-020-03095-2, URL http://link.springer.com/10.1007/s00348-020-03095-2.

Ottosson, P., Brown, M., Larsson, L., 2002. The effect of pitch radius of gyration on sailing Yacht performance. In: The Proceedings of the High Performance Yacht Design Conference. Auckland, New Zealand.

Persson, A., Larsson, L., Finnsgård, C., 2020. An improved procedure for strongly coupled prediction of sailing Yacht performance. In: The Proceedings of the 5th International Conference on Innovation in High Performance Sailing Yachts. Göteborg, Sweden.

Persson, A., Lindstrand, R., Muggiasca, S., Larsson, L., 2017. CFD prediction of steady and unsteady upwind sail aerodynamics. Ocean Eng. 141, 543–554. http://dx.doi.org/10.1016/j.oceaneng.2017.06.039.

Reissner, E., Stevens, J.E., 1947. Effect Of Finite Span On The Airload Distributions For Oscillating Wings 2: Methods Of Calculation And Examples Of Application. Technical Report NACA-TN-1195, National Advisory Committee for Aeronautics.

Roux, Y., Leroyer, A., Visonneau, M., Raymond, J., Hauville, F., 2008. Strongly coupled VPP and CFD RANSE code for sailing Yacht performance prediction. In: The Proceedings of the 3rd High Performance Yacht Design Conference. Auckland, New Zealand, pp. 215–226.

Singh, R., Baeder, J.D., 1997. Direct calculation of three-dimensional indicial lift response using computational fluid dynamics. J. Aircr. 34 (4), 465–471. http://dx.doi.org/10.2514/2.2214.

Spalart, P.R., Rumsey, C.L., 2007. Effective inflow conditions for turbulence models in aerodynamic calculations. AIAA J. 45 (10), 2544–2553. http://dx.doi.org/10.2514/1.29373.

Theodorsen, T., 1949. General Theory of Aerodynamic Instability and the Mechanism of Flutter. Technical Report NACA Report 496, National Advisory Committee for Aeronautics, Langley Memorial Aeronautical Laboratory.

Wagner, H., 1925. Über die Entstehung des dynamischen Auftriebes von Tragflügeln. ZAMM - Z. Angew. Math. Mech. 5 (1), 17–35. http://dx.doi.org/10.1002/zamm.19250050103.